Analysis of coastal eddies in the Gulf of Naples

BAGAGLINI LEONARDO*

Università degli Studi di Napoli Parthenope e Università degli Studi del Salento

ABSTRACT

We test three different eddy detection algorithms on HF radar datasets relative to the Gulf of Naples. The first two algorithms are adapted versions of those developed by Nencioli et al. in 2008 and by Le Vu et al. in 2017. The third novel method, designed for dealing with the problems arising from the highly non-geostrophy of the flow, is able to detect about 30% more eddies than the previous ones. We use these data to estimate the eddy boundary profiles and to describe the eddy spatial distribution.

Introduction

Among the various turbulent phenomena occurring in the ocean, submesoscale eddies are the most volatile ones, due to their short lifetime and length scale (within the ocean inertial range). They principally act as energy conveyors from the mesoscale to the microscale, but also play a crucial ecological role: they transport heat, nutrients and inorganic substances throughout small basins, influencing potentially entire ecosystems.

Submesoscale surface eddies, in particular, have characteristic lengths between 0.1 km and 10 km. They are completely confined in the surface mixed layer, within depths going from tens to hundreds metres. It is then clear that neither in situ measurements nor satellite observations can easily resolve the scales in which these phenomena occur. Moreover, since the relative Rossby and Froude numbers, Ro and Fr, are certainly not small, these structures show highly non-geostrophic behaviours; indeed they usually arise as perturbations of quasi-geostrophic balances. Despite such objective difficulties there is an increasing interest in their study, primary due to their profound influence on the local circulation just remarked and to the availability of finer observation technologies; in a recent survey McWilliams (2016) collected some of the main achievements obtained so far.

The Gulf of Naples is a small basin, with an area of 27 km times 32 km, located in a heavily anthropized site, so constantly analysed and monitored. However, despite the great amount of available data, no systematic studies of submesoscale surface eddies have been done before.

By means of a some existing, and novel, eddy detection algorithms, applied to HF radar observations of surface currents, we investigate the existence of submesoscale surface eddies which naturally inhabit the Gulf of Naples; we obtain estimates for their characteristic scale, shape and spatial distribution.

The article is structured as follows. In Section §1 we describe our dataset and in Section §2 we introduce the dynamical fields which allow us to identify whirling structures. Then in Section §3 we accurately describe the aforementioned detection algorithms, and in Section §4 we define a procedure for estimating eddy boundaries and radii. Finally in Section §5 we analyse the spatial distribution of the detected eddies.

1. The dataset

For this study we used the HF radar observations of surface currents in the Gulf of Naples, hereafter GoN, produced by a CODAR (Coastal Ocean Dynamics Application Radar) SeaSonde system. The product consists of a two-dimensional velocity field with a spatial resolution of 1.25 km over an area of approximately 20-30 km alongshore times 15-20 km offshore and with a hourly frequency (see Menna (2008) for more details on the apparatus and Paduan and Washburn (2013) for details concerning the HF radar theory and its applications to coastal currents observations). The reference time period, which counts 360 temporal frames, spreads from November 24 to December 8, 2008.

Since the observed GoN eddies have radii in a range between 0.5 and 5 km [1] we decided to refine the grid by

*E-mail: leonardo.bagaglini@gmail.com

Length: 11 pages.

Keywords: Surface currents; HF radar; detection algorithms.

[1] We found a mean *equivalent radius* of approximately 0.8 km, with extrema reaching 4 km.

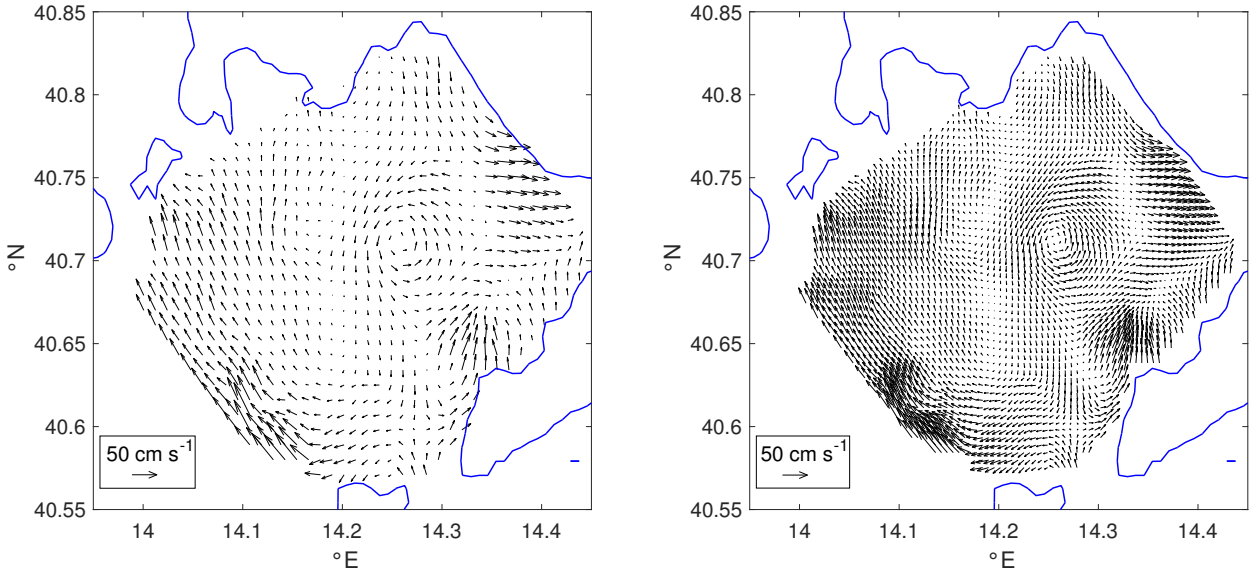

FIG. 1. Surface currents produced by the HF radar observations in the Gulf of Naples (on the left) and the interpolated data (on the right). Black arrows denote the velocity field whereas the blue line denotes the coastline.

increasing the spatial resolution up to approximately 0.5 km, by means of cubic interpolations, as illustrated in Figure 1.

Given a reference velocity scale U of $5\,\mathrm{cm\,s^{-1}}$, a length scale L of 0.5 km and a Coriolis parameter $f \sim 8.8 \cdot 10^{-5}\,\mathrm{s^{-1}}$, we obtain a Rossby number $\mathrm{Ro} \sim 0.6$. It is then evident that the quasi-geostrophic equations are not accurate for describing the GoN phenomena.

2. Dynamical fields

At first glance eddies of two-dimensional turbulent flows can be seen as regions characterized by a rigid-body rotation, and therefore many local, or semi-local, parameters can be adopted to decide whether vortices either exist or are likely to develop.

a. OW *and* LOW *parameters*

The Okubo-Weiss parameter OW is a local dynamical field which, loosely speaking, measures the relative dominance of the rate-of-strain tensor s over the vorticity ω of the velocity field[2]

$$\mathrm{OW} = |s|^2 - |\omega|^2.$$

It was independently introduced by Okubo (1970) and Weiss (1991). For a two-dimensional flow $\underline{u} = (u, v)$ it turns out that

$$\mathrm{OW} = \left(\frac{\partial}{\partial x}u\right)^2 + \left(\frac{\partial}{\partial y}v\right)^2 + 2\left(\frac{\partial}{\partial y}u\right)\left(\frac{\partial}{\partial x}v\right).$$

[2]Here $|.|$ denotes the euclidean module.

By definition it is evident that $\mathrm{OW} < 0$ whenever the rotation tendency exceeds the strain one.

We also define the *local* Okubo-Weiss parameter LOW (see Le Vu et al. (2017)). It depends on a positive distance $a > 0$ and is defined as the integral of OW over a ball of radius a:

$$\mathrm{LOW}(\underline{x}) = \int_{B_a(\underline{x})} \mathrm{OW}(\underline{x}')\,d\underline{x}'.$$

b. LNAM *and* LNMF *parameters*

In the rotating rigid-body analogy the angular momentum of a fluid particle has to be maximized about the eddy center, as pointed out by Mkhinini et al. (2014). This consideration suggested to define the local *normalized angular momentum field* LNAM:

$$\mathrm{LNAM}(\underline{x}) = \frac{\hat{z}\cdot\int_{B_a(\underline{x})}(\underline{x}'-\underline{x})\times\underline{u}\,d\underline{x}'}{\int_{B_a(\underline{x})}\left(|\underline{u}||\underline{x}'-\underline{x}| + |\underline{u}\cdot(\underline{x}'-\underline{x})|\right)d\underline{x}'}.$$

It assumes extreme values ± 1 at the centers of circular symmetric eddies; $+1$ for cyclonic rotations and -1 for anticyclonic ones[3].

Analogously we introduce the *local normalized momentum flux* field LNMF defined by

$$\mathrm{LNMF}(\underline{x}) = \frac{\int_{B_a(\underline{x})}\underline{u}\cdot(\underline{x}'-\underline{x})d\underline{x}'}{\int_{B_a(\underline{x})}\left(|\underline{u}||\underline{x}'-\underline{x}| + |\underline{u}\times(\underline{x}'-\underline{x})|\right)d\underline{x}'}.$$

It is clear that LNMF identically vanishes on centers of rotating eddies, while it assumes extreme values ± 1 in

[3]In Mkhinini et al. (2014) the term $\underline{u}\cdot(\underline{x}'-\underline{x})$ appears with its sign; we added the modulus to get $|\mathrm{LNAM}| \leq 1$.

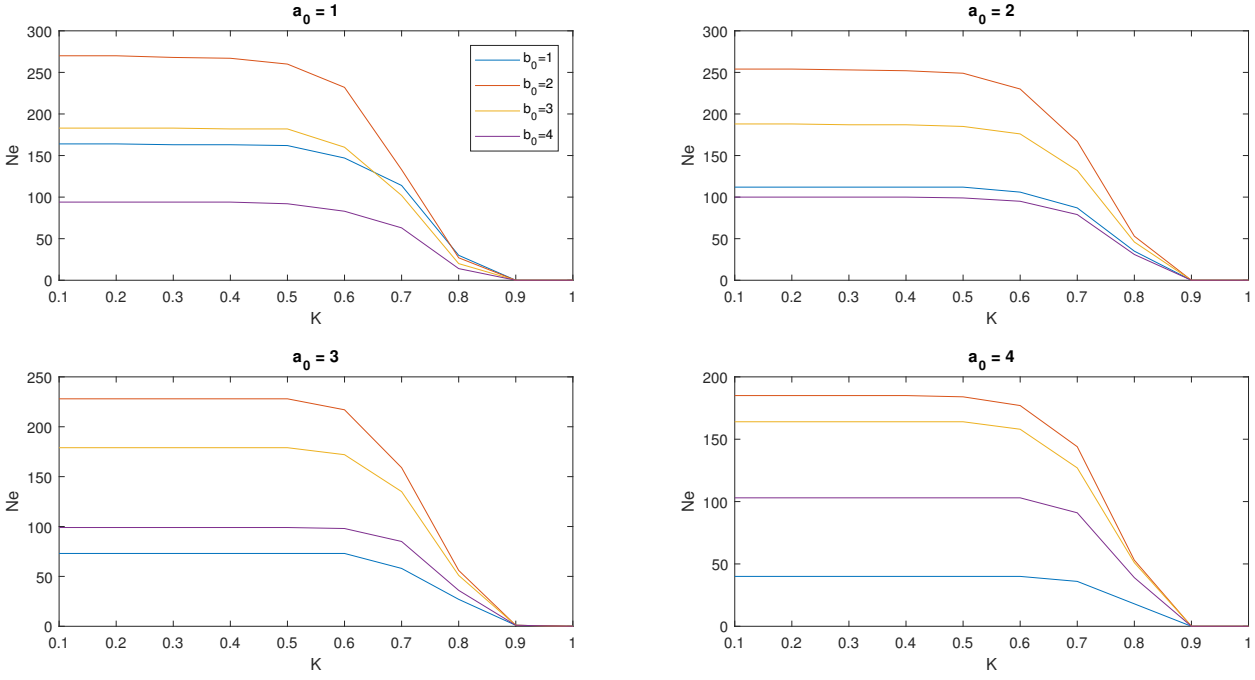

FIG. 2. Number of detected eddies Ne obtained with the algorithm M1 for different values of the parameters a_0, b_0 and K. In each figure, corresponding to a value of a_0, the coloured curves denote the graphs of Ne as a function of K for different values of b_0 (labelled as in the legend).

correspondence of symmetric sources and sinks; so it can be adopted to distinguish these various types of whirling structures.

3. Eddy detection methods

We decided to adopt three different methods for detecting GoN eddies:

M1 an adapted version of that developed by Le Vu et al. (2017);

M2 an adapted version of that developed by Nencioli et al. (2008);

M3 a third novel method inspired by Le Vu et al. (2017) and Post and Sadarjoen (2000).

The first method was tested on several products such as altimeter data, numerical simulations and laboratory experiments, while the second was specifically designed for certain HF radar datasets; it is important to note that in all cases the velocity fields were always geostrophic or quasi-geostrophic.

On the other hand the flow observed in the GoN is highly non-geostrophic and sensible variations of the divergence field frequently occur, often associated to whirling sources or sinks. So, in order to distinguish structures like these, it is necessary to refine the first two algorithms. The third method instead, as we will see, is precisely designed to deal with this issue.

a. Method 1

We can explicitly describe M1, as given in Le Vu et al. (2017), as follows:

1. look for grid points which are local extrema of LNAM satisfying LNAM $>$ K and LOW < 0, for a chosen threshold K $\in (0,1)$;

2. check the existence of at least one *closed* streamline around each extremum.

As we just pointed out the GoN eddies may have hyperbolic orbits, in contrast with the geostrophic flows of Le Vu et al. (2017) and Nencioli et al. (2008), and in such a case the second assumption is never verified. Then we adopted the following, already described by Nencioli et al. (2008):

2'. check that the velocity field constantly rotates along the perimeter of the square domain of edge $2b$ and centred at the extremum, for a chosen distance b.

The points so determined are considered centers of autonomous eddies.

Let us point out that, for numerical convenience, we substitute the ball $B_a(\underline{x})$ in the definition of LNAM and LOW with the square domain centred at $\underline{x}$ of edge $2a$, which we denote by Q_a. The second control is then performed on ∂Q_b as follows: following the path counterclockwise we check that any velocity vector at a given grid

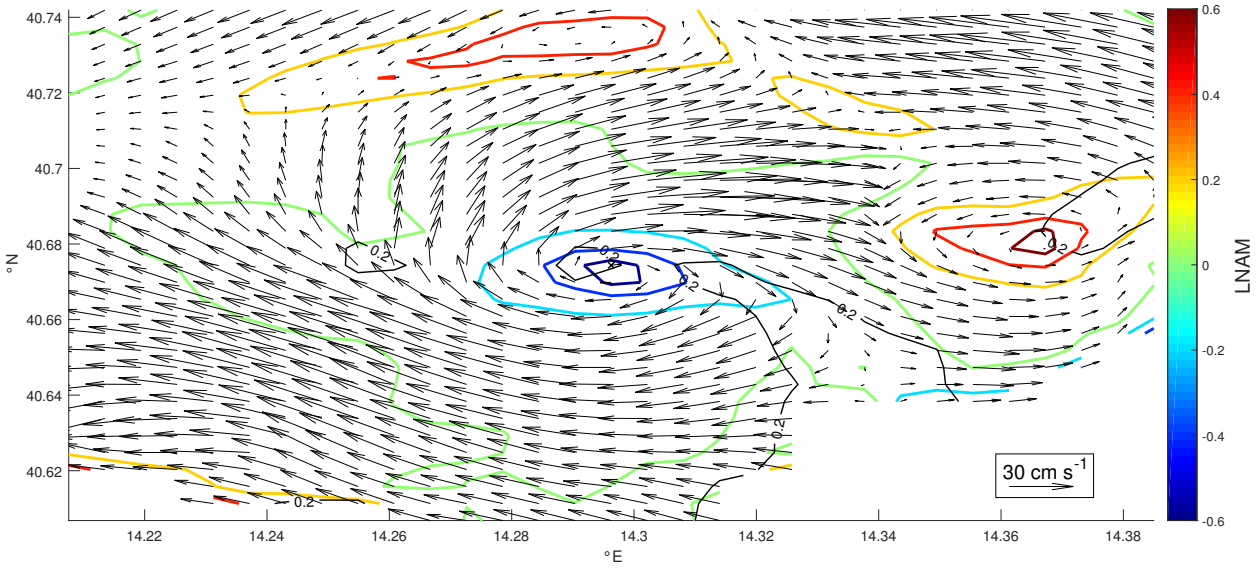

FIG. 3. Source-like eddy core detected by the algorithm M1 (black cross), velocity field (black arrows), Local Normalized Angular Momentum field LNAM contour lines (coloured) and Local Normalized Momentum Flux LNMF = 0.2 contour (black lines).

point is rotated at the left of the previous by an angle less than $\pi/2$ radians; note that this criterion does not depend on the sense of rotation of the velocity field along the path.

We note that there are three parameters to be determined: a, from the definition of LNAM and LOW, K and b. To obtain all dimensionless parameters we divide a and b by the length scale l of one pixel ($l \sim 0.5$ km)[4]: $a_0 = a/l$ and $b_0 = b/l$.

Of course the optimal choice of these parameters depends on the scale analysis relative to the GoN: if a_0 is too large then LNAM may sum up the contribution of many eddies inside Q_a, leading to a wrong estimate of the angular momentum; similarly a large b_0 is not recommended, nor a small one since the velocity vector may abruptly rotate with an angular velocity greater than $\pi/2$ radians per pixel in proximity of the eddy center; the parameter K, in turn, once a_0 is coherently chosen, represents a lower bound for the detected eddy intensity.

We ran the algorithm on all the dataset for different values of the parameters a_0 and b_0, and analysed the number of detected eddies Ne as a function of K, varying from 0.1 to 1 with step 0.1. The results are shown in Figure 2.

For any choice of a_0 and b_0 the values of Ne turn out to be approximately constant in $\mathrm{K} < 0.6$, so we can safely fix $\mathrm{K} = 0.6$. On the other hand for a fixed a_0 the maximum of Ne is achieved at $b_0 = 2$; so let us choose this value for b_0. Finally we see that Ne weakly decreases as a_0 increases, as expected, suggesting to take $a_0 = 1$. Summarizing our optimal choice of the parameters turns out be $(a_0, b_0, \mathrm{K}) = (1, 2, 0.6)$.

[4]Since longitudinal and latitudinal resolutions do not exactly coincide we chose l as the minimum value.

As we already noticed the non-geostrophy of the flow makes possible the existence of whirling structures which do not effectively entrap fluid masses; mainly because of divergences spread throughout the rotating region (see for instance the flow structure in Figure 3) Since we are interested in discarding these particular structures we add a third control to M1:

3. discard those extrema satisfying LNMF > 0.2.

In other words we allow only a little divergence near the eddy core; see the LNMF contour line in Figure 3. This correction reduces the number of detected eddies Ne by about 16% for $\mathrm{K} = 0.6$, and by 0.4% for $\mathrm{K} = 0.7$; this behaviour is expected since strong rotations often imply weak divergences.

Unfortunately this criterion is not optimal: it is a pure dynamical control depending on the local behaviour of the flow, but eddies are extensive structures which may admit internal divergences. In such a case the eddy center and its real extension are difficult to estimate since it would be necessary to understand the streamline geometry. We will try to do this through the definition of M3.

b. Method 2

Let us briefly describe M2, as developed by Nencioli et al. (2008):

1. look for couples of grid points $(\underline{x}_1, \underline{x}_2)$ such that the meridional component of the velocity field changes sign going westward along the zonal segment of length $2a$, centred at $\underline{x}_i$, and increases its magnitude away from this point. This computation also provides the expected sign of rotation;

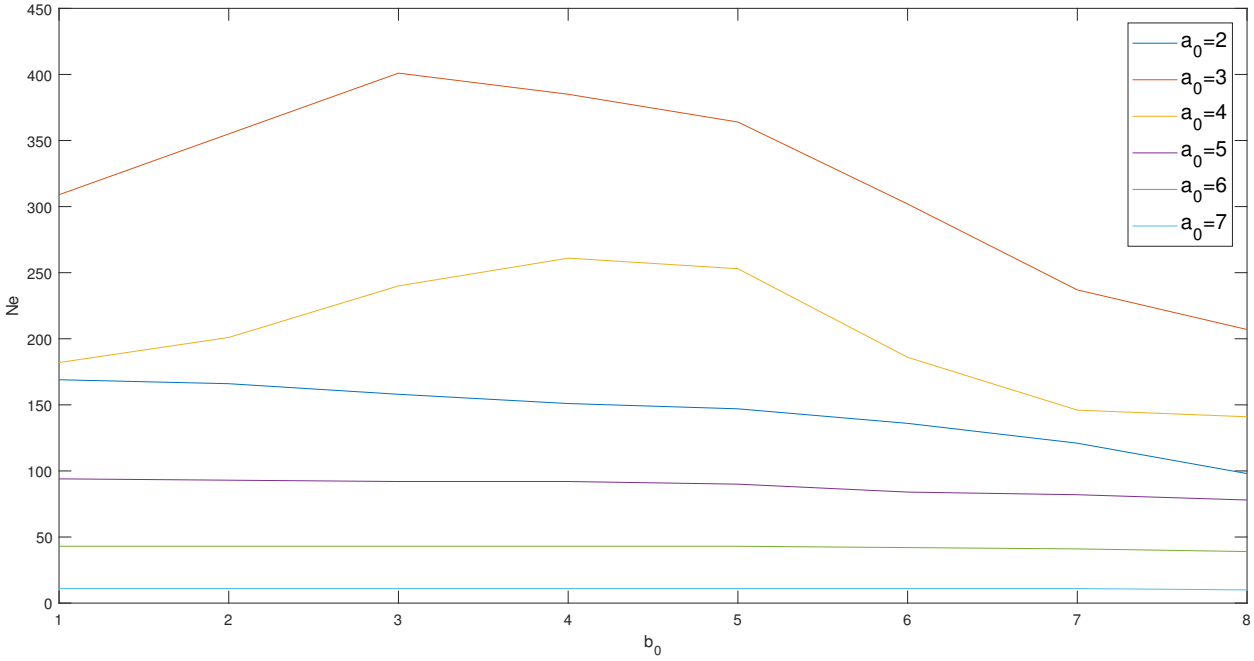

FIG. 4. Number of detected eddies Ne obtained by the algorithm M2 with respect to different choices of the parameters a_0 and b_0. Coloured lines denote the graphs of Ne as a function of b_0 for different values of a_0 (labelled as in the legend).

2. check that, at any such grid point $\underline{x}_i$, the zonal component of the velocity field changes sign going northward along the meridional segment of length $2a$, centred at $\underline{x}_i$, and increases its magnitude away from this point. This change must be compatible with the expected rotation;

3. look for the KE (kinetic energy) local minima inside a square domain of edge $2b$, centred at $\underline{x}_i$, which are global minima in a square neighbourhood Q_b of the same size;

4. check that the velocity field constantly rotates along the perimeter ∂Q_b.

By definition M2 turns out to be a purely geometrical method, which does not require to compute any differential quantity: eddy centers are simply defined as energy minima. Of course this reduces the computation time, making the algorithm considerably svelte and efficient. Moreover we note that, as in the previous case, there are two parameters, a and b, to be determined for tuning; as before let us consider the dimensionless parameters $a_0 = a/l$ and $b_0 = b/l$.

We ran the algorithm on the dataset for $a_0 = 1,\dots,8$ and $b_0 = 1,\dots,8$. Discarding the unlikely results obtained for $a_0 = 1$ (Ne > 1000) what remains is shown in Figure 4. We see that for $a_0 = 2$ there is a weak dependence on b_0, but the values of Ne turn out to be much less than that obtained by M1. For $a_0 = 3,4$ the number of detected eddies highly depends on b_0, but the results does not clearly converge anywhere; for $a_0 > 4$ we obtained values depending weakly on b_0 but much less than those for $a_0 = 2$. These discrepancies are likely caused by asymmetrical eddies having not radially increasing velocity components. In conclusion it seems that M2 can not be easily tuned to work with our dataset.

c. *Method 3*

M3 is based on the following idea: take the local extrema of a dynamical field, e.g. LNAM, KE or OW, and then study the streamline geometry inside some neighbourhood, ensuring the existence of either bounded hyperbolic orbits (characterizing eddies with sink-like cores) or elliptic orbits (in presence of eddies having stable orbits).

We begin by detecting any local extremum $\underline{x}$ of LNAM satisfying LNAM > 0.6 for $a_0 = 1$; having tested this values in tuning M1. We then consider a square neighbourhood Q_b centred at $\underline{x}$ with edge $2b$ (we chose $b = 10l$); the length b has to be intended as an upper limit for the eddy radius. Within this domain we define a circle C_r of radius $r = l$, centred at $\underline{x}$ and composed by 8 points (as many as the grid points on the tangent square perimeter). We use cubic interpolations to draw the streamlines emanated by these points[5], collecting their mean points (geometric mean) and end points.

[5] Each streamline is built by means of an Euler's method with a step of 5 points per pixel and is composed by up to 1000 points (MATLAB routine *stream2*).

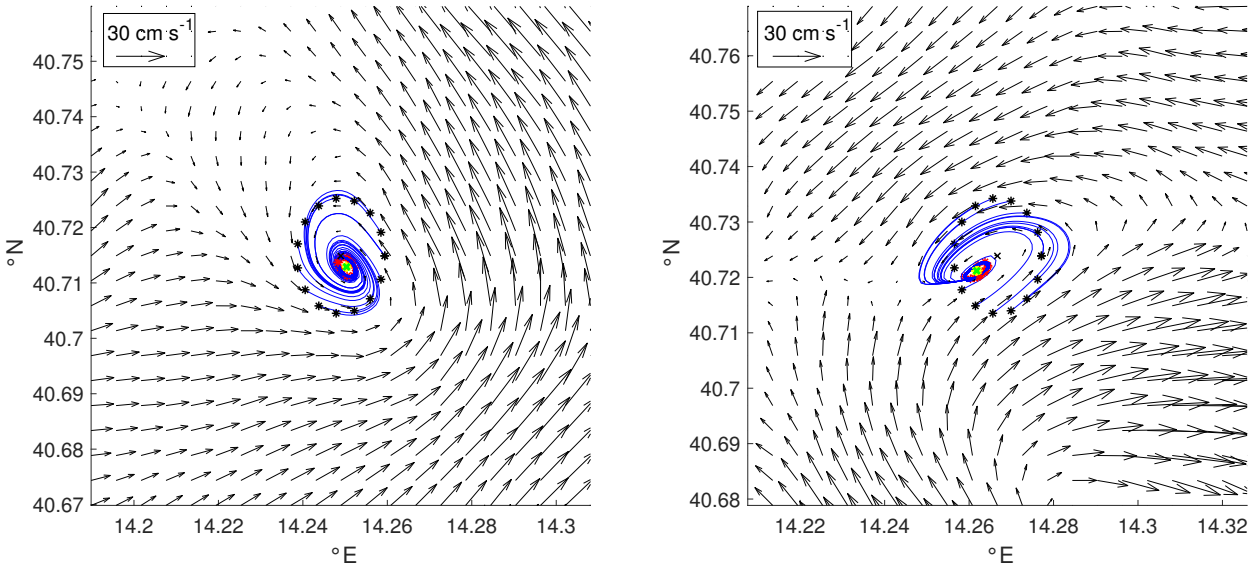

FIG. 5. Maps showing the functioning of the algorithm M3 for two eddies with sink-like cores. Once the Eddy Extreme Point EEP (black crosses) is detected, M3 looks for a circle (black stars), centred at the extremum, which emanates streamlines (blue lines) with the following property: the streamline has to complete up to a revolution without reaching the domain boundary. Then it evaluates the mean points (yellow stars) and end points (red stars) of such streamlines, choosing the mean point of the second distribution as Eddy Symmetry Center ESC (green stars). Black arrows denote the velocity field.

We then select all the streamlines such that 1) the end points belong to the square domain Q_{b-2l} (that is they stay away from the boundary of the reference domain) and 2) each streamline completes at least one revolution. This last property is checked by looking at the *cumulative winding-angle*[6] of the streamline, as defined by Post and Sadarjoen (2000): it has to be, in modulus, equal to or grater than 2π. If no such streamline exists we increase the radius of C_r by l until at least one streamline satisfying 1) and 2) is found; the maximum allowable r will be $b/2$ (at any step we increase the number of points in the circle to match the amount of grid points in the tangent square perimeter).

Note that if one such streamline exists it means that either it converges to some point inside the domain or it definitely stays inside the domain without converging anywhere (at least for the first 1000 points). Of course it could exists some diverging streamline which rotates without reaching the boundary of the domain, and then taken by the algorithm. But a path starting from $\underline{x}$ which rotates around it at least 3 times before reaching the boundary, and having the same step-size of the drawn streamlines, counts approximately 300-400 points: so, if a spiral-like streamline diverging from the center stays inside the domain without reaching the boundary, then it has to complete at least 8 revolutions; even in this case we can safely affirm that an eddy exists.

Once we have selected the streamlines satisfying 1) and 2) for the first allowable r, we compare the distributions of the mean points with that of the end points. If the eddy core behaves as a sink all the end points will accumulate near it, on the other hand if the orbits around the eddy are elliptic the mean points will do. So we choose the distribution with less variance and choose its mean point as eddy barycenter or *eddy symmetry center*, shortly ESC; by contrast the extremum will be called the *eddy extreme point*, hereafter EEP. However, to ensure us we are not selecting another eddy in the square domain relative to a different extremum, we check that the expected ESC belongs to the disk bounded by C_r, otherwise we discard the point and we move to the next extremum; samples can be found in figures 5 and 6.

Generally the ESC does not coincide with the eddy center even though it provides a better approximation of the true eddy core than the EEP; e.g. figures 5, 6, 8 and 9. As consequence the distance between the ESC and the EEP can be though as a measure of the eddy asymmetry.

The algorithm so defined computed a number of detected eddies Ne equal to 255, about 30% more than the value obtained with M1. Eddies as those in Figure 5, for instance, are missed by M1 due to their small extension and asymmetry, whereas they are detected by M3. However there are still structures detected by M1 and missed by M3, see for instance Figure 7. In some of these cases we noted that the divergence around the LNAM extremum

[6]Given an oriented piece-wise linear curve, its cumulative winding-angle is the sum, over all the angular points, of the angle (with positive sign going counter-clockwise and negative going clockwise) between the two intersecting segments, considered as vectors.

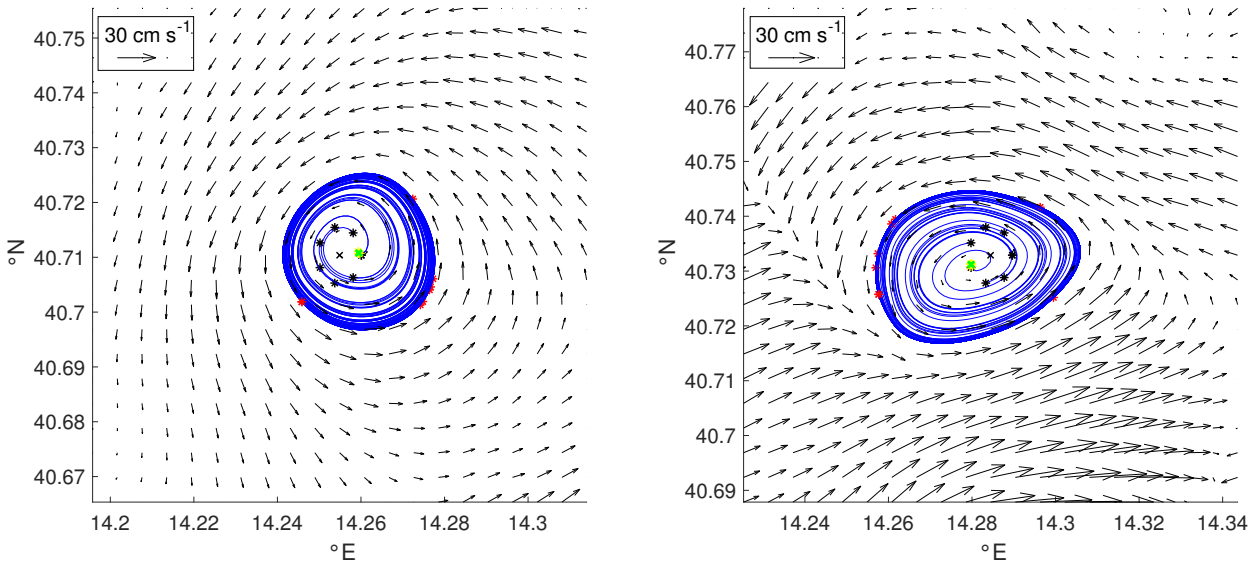

FIG. 6. Maps showing the functioning of the algorithm M3 for two eddies having elliptic orbits. Once the Eddy Extreme Point EEP (black crosses) is detected, M3 looks for a circle (black stars) emanating streamlines (blue lines) with the following property: each streamline has to complete up to a revolution without reaching the domain boundary. Then it evaluates the mean points (yellow stars) and end points (red stars) of such streamlines, choosing the mean point of the first distribution as Eddy Symmetry Center ESC (green stars). Black arrows denote the velocity field.

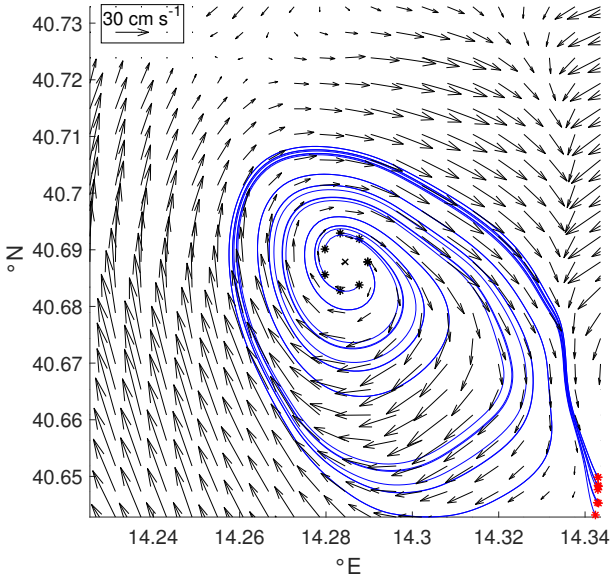

FIG. 7. Eddy detected by M1 and missed by M3. The Local Normalized Angular Momentum field LNAM extremum x (black cross) corresponds to an eddy core, but any circle centred at x (black stars) emanates streamlines (blue lines) which complete up to 3 revolutions before reaching the domain boundary (contact points in red). Black arrows denote the velocity field.

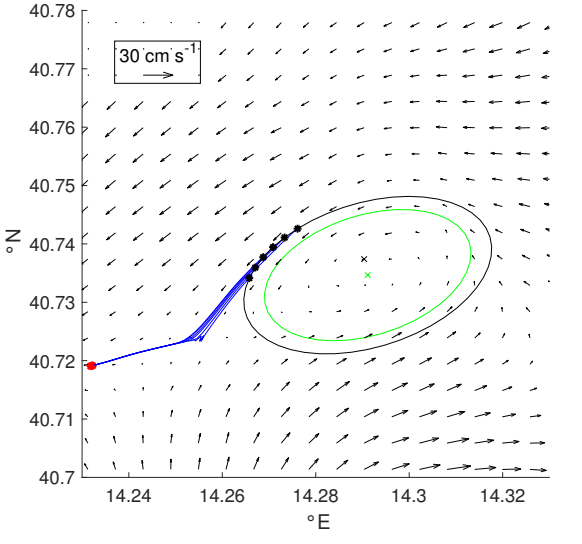

FIG. 8. Map showing the boundary computation of an eddy having a sink-like core. Once the Eddy Extreme Point EEP (black cross) and the Eddy Symmetry Center ESC (green cross) are detected the algorithm draws the ellipses centred at the ESC with increasing radii. The cycle breaks when the black ellipse is drawn due to the existence of inamissible streamlines (blue lines) leaving the domain. The last computed ellipse (green line) will be considered as boundary. Black arrows denote the velocity field.

is so weak (LNMF < 0.2) that some orbits complete up to three revolutions before leaving the region.

In conclusion we can affirm that M3 is able to detect and distinguish multiple kinds of eddies and, as we will see in the next section, it can be refined to estimate their boundaries.

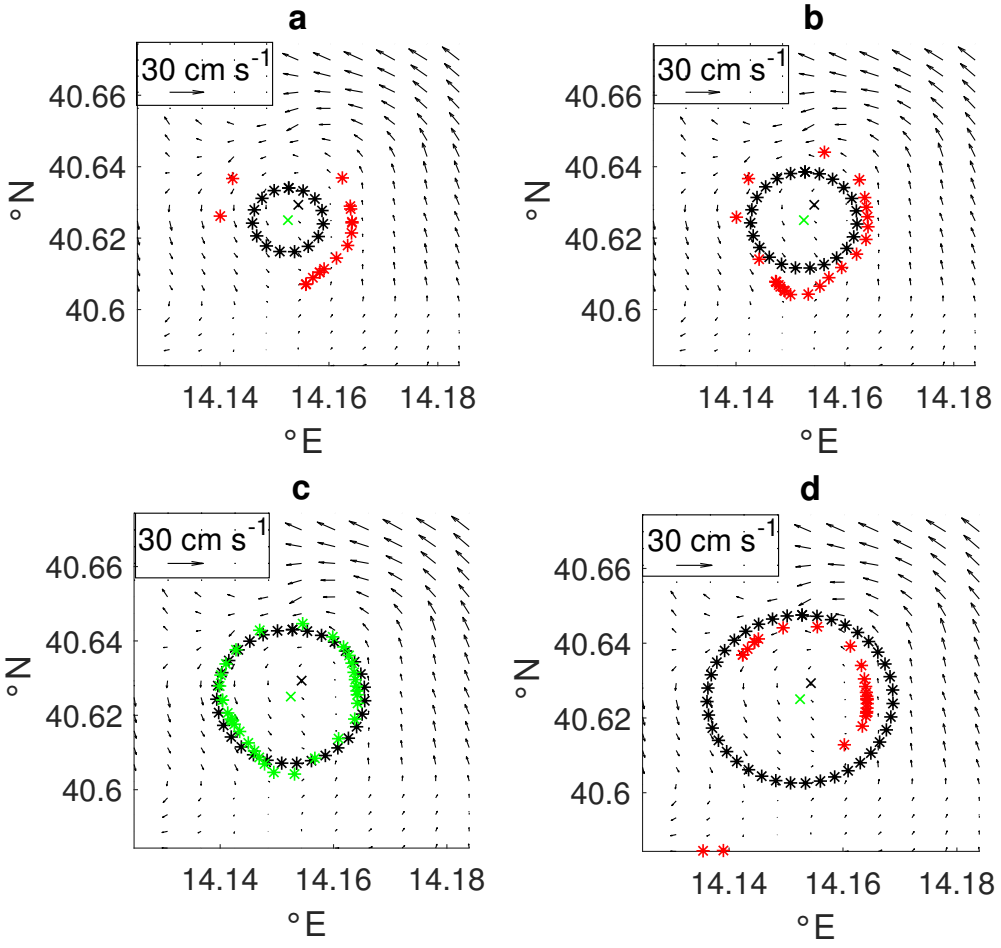

FIG. 9. Maps showing the boundary computation of an eddy having stable orbits. Once the Eddy Extreme Point EEP (black crosses) and the Eddy Symmetry Center ESC (green crosses) are detected the algorithm draws the ellipses centred at the ESC with increasing semi-major axis d (black stars); from figures a to d the semi-major axis increases from 2 to 5 pixel lengths. It then evaluates the end points (red stars in figures a,b and d, and green stars in c) of the streamlines emanated by these ellipses. The algorithm selects the semi-major axis d^* for which the relative end points (green stars in c) form the closest deformation of the associated ellipse. Black arrows denote the velocity field.

4. Boundaries

There is no a universal definition of eddy boundary: many authors adopted OW or ω contour lines, as well as closed streamlines or closed stream-function contours (not equivalent at all) to locate them.

Keeping in mind the functioning of M3 we propose a different definition, which aims to distinguish eddies with sink-like cores from those having elliptic orbits. Of course we can not expect to identify the true boundary profile, so we assume it to be elliptic (rather than circular).

a. Sink-like cores

We consider the set S_r of all the streamlines emanated by C_r and satisfying conditions 1) and 2) as explained in the definition of M3. We then evaluate the variance ellipse of this distribution of points; let e be its eccentricity. We then draw the ellipse E_d of eccentricity e, centred at the ESC, with major semi-axis $d = l$. As we did for C_r we consider the streamlines emanated by E_d: if all such streamlines belong to the ellipse interior we increment d by l, repeating the step up to reach $d = b$. Further, in analogy with Le Vu et al. (2017), we also control that the circulation along E_d does not decrease by increasing d. The largest ellipse E_d satisfying this criterion will define the eddy boundary; as shown in Figure 8.

b. Eddies having elliptic orbits

For such eddies we also start by building the variance ellipse of the admissible streamlines S_r. Then we draw the ellipses E_d with eccentricity e, centred at the ESC and having semi-major axis $d = l, 2l, \ldots, d'$, where d' is the maximum distance for which the circulation around E_d is a non-decreasing function of d, and we move each E_d

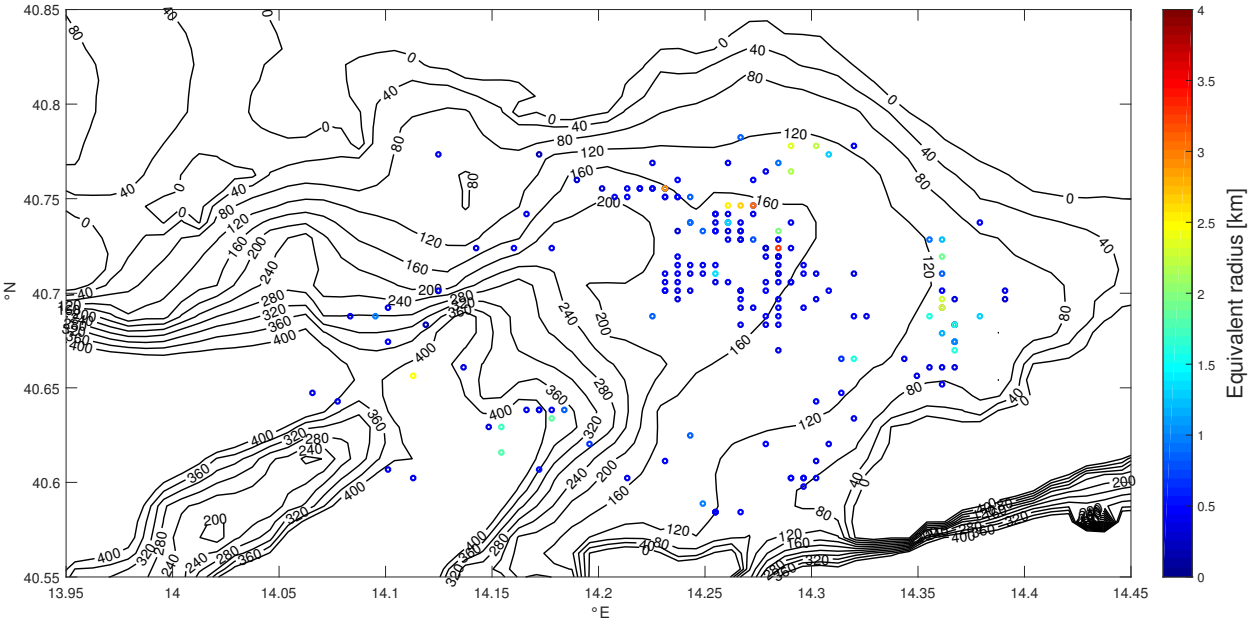

FIG. 10. Spatial distribition of the detected eddies by means of M3. Detected eddies (coloured circles) and bathymetric contour lines (black lines) between 0 m and 400 m of depth; different colors denote different sizes. Bathymetry data: 30 arc-sec interval grid GEBCO_ 2014 Grid, from the General Bathymetric Chart of the Ocean (GEBCO).

following the flow: in other words we collect all the end points of the streamlines emanated by E_d; let us denote this set by $\varepsilon(E_d)$.

We expect that, if E_d approximates the eddy boundary, it has to be close to an elliptic orbit, and therefore $\varepsilon(E_d)$ has to be a small deformation of E_d. However to ignore effects of translating motions, which may occur, we center the two sets at the same reference point. Then we evaluate the Hausdorff distance $\delta(d)$ between them (see the Appendix for details).

Finally we take d^* satisfying $\delta(d^*) = \min\{\delta(d)\}$, and E_{d^*} as eddy boundary; we choose E_{d^*} to maintain the elliptic symmetric, though $\varepsilon(E_{d^*})$ would provide a better approximation. In Figure 9 we plotted the various steps just described.

c. *Equivalent radii*

Following Le Vu et al. (2017) we computed the *equivalent radius* ρ for each detected eddy. It is defined as the radius of the circle bounding an area equivalent to that delimited by the eddy boundary; for elliptic contours it equals $d\sqrt[4]{1-e^2}$. A statistical analysis have shown that the mean radius $\bar{\rho}$ relative to the sample data equals 0.87 km, with a standard deviation of 0.84 km and values of 2.8 and 3.6 km for the 95th and 99th percentile respectively. Similarly we computed a mean eccentricity $\bar{e}$ of 0.71 with standard deviation of 0.02. It turns out that the mean equivalent radius is merely 1-2 times the pixel length scale of the dataset, and therefore we may expect that our method will not accurately describe some kinematic and dynamic features of eddies having ρ close to $\bar{\rho}$. Maybe it would be possible to obtain a more accurate description by increasing the spatial resolution up to reach $l \sim 0.3$ km; however this would imply to perform more invasive interpolations.

5. Spatial distribution

Recall that the dataset temporal resolution is about 1h, and that some eddies may have longer lifetimes. To track such long-lived structures we checked whether each eddy has some other EEP, relative to the previous temporal frame, encircled by its boundary. The spatial distribution of all the detected eddies, counted without repetitions, is represented in Figure 10.

We can appreciate a larger density in correspondence of a relatively flat plateau sited in 40.73°N, 14.27°E, between 120 and 160 metres of depth, excluding topographic wakes as primary instability causes (see also McWilliams (2016)). To understand the instability sources generating the GoN eddies, therefore, it would be necessary to investigate the flow behaviour within the SBL (surface boundary layer). Unfortunately there are neither wind observations nor density profiles relative to the GoN SBL. However, there is a work in progress, funded by the Science and Technology department of the University of Napoli Parthenope, aiming to investigate the vertical water profile through numerical simulation. Such a study could provide

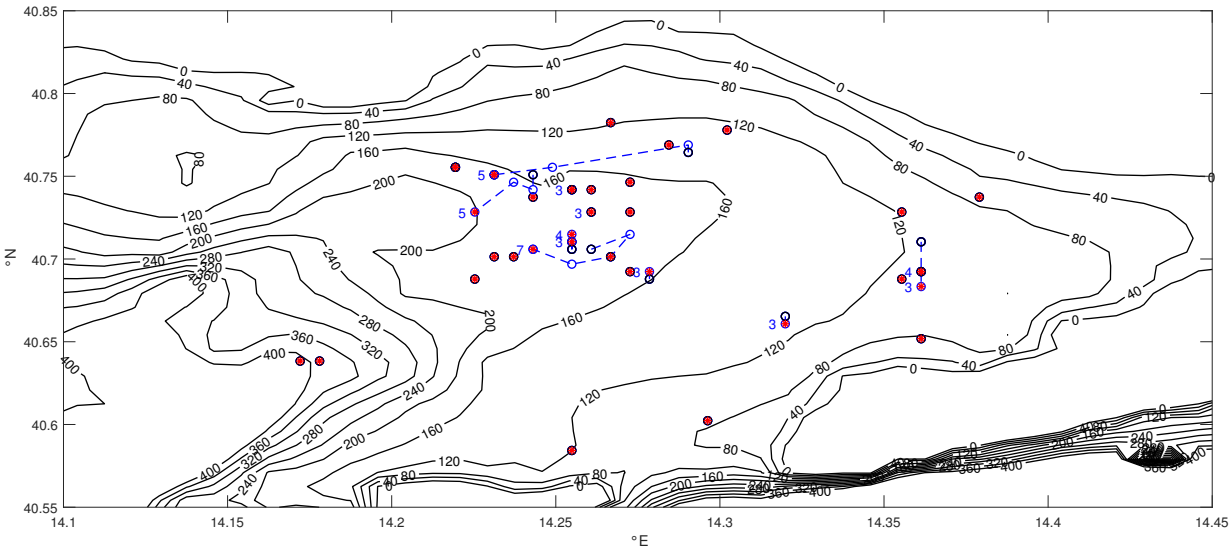

FIG. 11. Map of detected long-lived eddies by means of M3. Detected long-lived eddies (circles) with lifetime $T \geq 2$h. Initial, mid and final Eddy Extreme Points EEPs (black circles, blue circles and red stars respectively) with their relative eddy trajectories (blue dashed lines) and eddy lifetimes $T \geq 3$h (blue numbers). Bathymetry as in Figure 10.

more informations to understand the instability sources within the GoN.

Finally we may observe that the detected long-lived eddies, namely those with lifetimes greater than 1h, are 36, distributed as shown in Figure 11. They usually persist for few hours, 5 or 7 hours in some cases, and their spatial distribution agrees with that of Figure 10. We also note that, except for few examples, they seem to be almost stationary.

Conclusions

We tuned the algorithm M1 to our dataset observing that, though reliable, it was not able to distinguish eddies entrapping fluid masses from the others. So we refined the algorithm by measuring the divergence occurring in the eddy core; the number of detected eddies then decreased from 233 to 196. Differently we did not succeed to tune the algorithm M2 for working in our dataset.

To obtain a more efficient detection method, able to distinguish asymmetric eddies entrapping fluid masses, we developed the algorithm M3, which detected 255 eddies (about 30% more than the refined M1 value). Then we used M3 to estimate the eddy boundaries, assuming an elliptical symmetry, and we found a mean equivalent radius of 0.87 km and a mean eccentricity of 0.71.

Finally, looking at the spatial distribution of the detected eddies, we observed a larger density in correspondence of a plateau sited at 160m of depth, excluding topographic wakes as main instability sources.

Acknowledgments. The author is grateful to Prof. E. Zambianchi for having suggested the argument and for several helpful comments and improvements. Also, he wants to thank Daniela, Edoardo, Francesco, Luca and Roberto for many pleasant conversations they shared with him.

APPENDIX

The Hausdorff distance

The Hausdorff distance $\delta_H(A,B)$ between two compact subsets A and B of the euclidean plane is defined by the formula

$$\delta_H(A,B) = \max\left\{\sup_{a\in A} d(a,B), \sup_{b\in B} d(b,A)\right\},$$

where $d(a,B)$ and $d(b,A)$ are the usual point-set distances:

$$d(a,B) = \inf_{b\in B}|a-b|, \quad d(b,A) = \inf_{a\in A}|b-a|.$$

The Hausdorff distance δ_H makes the set of all compact subsets a metric space; in particular $\delta_H(A,B) = 0$ if and only if $A = B$.

References

Le Vu, B., A. Stegner, and T. Arsouzea, 2017: Angular Momentum Eddy Detection and tracking Algorithm (AMEDA) and its application to coastal eddy formation. *Atmospheric and Oceanic Technology*, **35**, 739–762, doi:10.1175/JTECH-D-17-0010.1.

McWilliams, J., 2016: Submesoscale currents in the ocean. *Proc. R. Soc. A 472: 20160117*, doi:10.1098/rspa.2016.0117.

Menna, M., 2008: Misure di correnti superficiali nel Golfo di Napoli eseguite con radar costiero. *Università degli Studi di Napoli Federico II*, doi:10.6092/UNINA/FEDOA/2660, ph.D. thesis.

Mkhinini, N., A. L. S. Coimbra, A. Stegner, T. T.-L. Arsouze, I., and K. Béranger, 2014: Long-lived mesoscale eddies in the eastern Mediterranean Sea: Analysis of 20 years of AVISO geostrophic velocities. *J. Geophys. Res. Oceans*, **119**, 86038626, doi:10.1002/2014JC010176.

Nencioli, F., C. Dong, T. Duckey, L. Washburn, and J. C. McWilliams, 2008: A Vector GeometryBased Eddy Detection Algorithm and Its Application to a High-Resolution Numerical Model Product and High-Frequency Radar Surface Velocities in the Southern California Bight. *J. of Atmospheric and Oceanic Technology*, **27**, 564–579., doi:10.1175/2009JTECHO725.1.

Okubo, A., 1970: Horizontal dispersion of floatable trajectories in the vicinity of velocity singularities such as convergencies. *Deep-Sea. Res.*, **17**, 445454.

Paduan, J. D., and L. Washburn, 2013: High-Frequency Radar Observations of Ocean Surface Currents. *Annu. Rev. Mar. Sci.*, **5**, 115136, doi:10.1146/annurev-marine-121211-172315.

Post, F. H., and I. A. Sadarjoen, 2000: Detection, quantification, and tracking of vortices using streamline geometry. *Computers & Graphics*, **24**, 333–341.

Weiss, J., 1991: The dynamics of enstrophy transfer in 2-dimensional hydrodynamics. *Physica D.*, **48**, 273294.